CHARACTERIZATION OF MATERIALS

SECOND EDITION

Volume 2

Editor-in-Chief

Elton N. Kaufmann
Argonne National Laboratory
Argonne, IL

Characterization of Materials is available Online in full color
at www.mrw.interscience.wiley.com/com.

⊛WILEY

CONTENTS, VOLUMES 1, 2, AND 3

RESONANCE METHODS

9

JOSEPH P. HORNAK, Chapter Editor

Rochester Institute of Technology, Rochester, NY, USA

Contents

COM

CYCLOTRON RESONANCE

D. J. Hilton,[1] T. Arikawa,[2] and J. Kono[2]

[1]University of Alabama, Birmingham, AL, USA
[2]Rice University, Houston, TX, USA

INTRODUCTION

Cyclotron resonance (CR) is a method for measuring the effective masses of charge carriers in solids. It is by far the most direct and accurate method for providing such information. In the simplest description, the principle of the method can be stated as follows. A particle of effective mass m^* and charge e in a DC magnetic field B executes a helical motion around B with the cyclotron frequency $\omega_c = eB/m^*$. If, at the same time, an AC electric field of frequency $\omega = \omega_c$ is applied to the system, perpendicular to B, the particle will resonantly absorb energy from the AC field. Since B and/or ω can be continuously swept through the resonance and known to a very high degree of accuracy, m^* can be directly determined with high accuracy by $m^* = eB/\omega$.

In crystalline solids, the dynamics of charge carriers (or Bloch electrons) can be most conveniently described by the use of the effective mass tensor, defined for simple nondegenerate bands as

$$(\overline{m})_{\mu\nu} = \left(\frac{1}{\hbar^2} \frac{\partial^2 E(\vec{k})}{\partial k_\mu \partial k_\nu} \right)^{-1} \quad (\mu, \nu = 1\text{-}3) \quad (1)$$

where $E = E(\vec{k})$ is the energy dispersion relation near the band edge ($\vec{p} = \hbar\vec{k}$ is the crystal momentum). Hence, the primary purpose of CR in solids is to determine the components of the effective mass tensor, or the curvature of the energy surface, at the extrema of the conduction and valence bands (or at the Fermi surface in the case of a metal). In the 1950s, the first CR studies were carried out in germanium and silicon crystals (Dresselhaus et al., 1953, 1955; Lax et al., 1953), which, in conjunction with the effective mass theory (e.g., Luttinger and Kohn, 1955; Luttinger, 1956), successfully determined the band-edge parameters for these materials with unprecedented accuracy. Since then, CR has been investigated in a large number of elementary and compound materials and their alloys and heterostructures.

Quantum mechanically, the energy of a free electron in a magnetic field is quantized as $E_N = (N + 1/2)\hbar\omega_c$, where $N = 0, 1, 2, \ldots, \infty$ and $\hbar\omega_c$ is called the cyclotron energy. These equally spaced energy levels, or an infinite ladder, are the well-known Landau levels (see, e.g., Kittel, 1987). At high magnetic fields and low temperatures (T), where $k_B T < \hbar\omega_c$ (k_B is the Boltzmann constant), this magnetic quantization becomes important, and CR may then be viewed as a quantum transition between adjacent Landau levels ($\Delta N = \pm 1$).

In real solids, Landau levels are generally not equally spaced since the energy dispersion relation, E versus k, is not generally given by a simple parabolic dispersion relation $E(\vec{k}) = \hbar^2|\vec{k}|^2/2m^*$. The degree of nonparabolicity and anisotropy depends on the material, but, in general, the effective mass is energy dependent as well as direction dependent. Landau levels for free carriers in solids cannot be obtained analytically, but several useful approximation models exist (e.g., Luttinger, 1956; Bowers and Yafet, 1959; Pidgeon and Brown, 1966). These calculations could be complex, especially when one is concerned with degenerate bands such as the valence bands of group IV, III–V, and II–VI semiconductors. However, a detailed comparison between theory and experiment on quantum CR can provide a critical test of the band theory of solids (e.g., Suzuki and Hensel, 1974; Hensel and Suzuki, 1974).

As a secondary purpose, one can also use CR to study carrier scattering phenomena in solids by examining the scattering lifetime τ (the time between collisions, also known as the collision time or the transport/momentum relaxation time), which can be found from the linewidth of CR peaks. In the classical regime, where most electrons reside in states with high Landau indices, τ is directly related to the static (or DC) conductivity in the absence of the magnetic field. The temperature dependence of τ then shows markedly different characteristics for phonon scattering, impurity scattering, and scattering from various imperfections. However, in the quantum regime, where most electrons are in the first few Landau levels, the effect of the magnetic field on scattering mechanisms is no longer negligible, and τ loses its direct relationship with the DC mobility (for theory, see, e.g., Kawabata, 1967).

As the frequency of scattering events (or the density of scatterers) increases, CR linewidth increases, and, eventually, CR becomes unobservable when scattering occurs too frequently. More quantitatively, in order to observe CR, τ must be long enough to allow the electron to travel at least $1/2\pi$ of a revolution between two scattering events, that is:

$$\tau > \frac{T_c}{2\pi} = \frac{1}{\omega_c}$$

or

$$\omega_c \tau = \frac{eB}{m^*}\tau = \frac{e\tau}{m^*}B = \mu B > 1 \quad (2)$$

where T_c is the period of cyclotron motion and $\mu = e\tau/m^*$ is the DC mobility of the electron. Let us examine this CR observability condition for a realistic set of parameters. If $m^* = 0.1 m_0$ (where $m_0 = 9.1 \times 10^{-31}$ kg) and $B = 1$ T, then $\omega_c = eB/m^* \approx 2 \times 10^{12}$ s^{-1}. Thus, one needs a microwave field with a frequency of $f_c = \omega_c/2\pi \approx 3 \times 10^{11}$ Hz $= 300$ GHz (or a wavelength of $\lambda_c = c/f_c \approx 1$ mm). Then, in order to satisfy Equation 2, one needs a minimum mobility of $\mu = 1$ m^2/(V s) $= 1 \times 10^4$ cm^2/(V s). This value of mobility can be achieved only in a limited number of high-purity semiconductors at low temperatures, thereby posing a severe limit on the observations of microwave CR.

From the resonance condition $\omega = \omega_c$, it is obvious that if a higher magnetic field is available (see GENERATION AND MEASUREMENT OF MAGNETIC FIELDS), one can use a higher frequency (or a shorter wavelength), which should make Equation 2 easier to satisfy. Hence, modern CR methods almost invariably use far-infrared (FIR) (or terahertz (THz)) radiation instead of microwaves (Kono and Miura, 2006). Strong magnetic fields are available either in pulsed form (up to $\sim 10^3$ T) or in steady form by superconducting magnets (up to ~ 20 T), water-cooled magnets (up to ~ 30 T), or hybrid magnets (up to ~ 45 T). In these cases, even at room temperature, Equation 2 may be fulfilled. Here we are only concerned with the methods of FIR-CR. The reader particularly interested in microwave CR is referred to Lax and Mavroides (1960).

Although this article is mainly concerned with the simplest case of free carrier CR in semiconductors, one can also study a wide variety of FIR magneto-optical phenomena with essentially the same techniques as CR. These phenomena ("derivatives" of CR) include: (a) spin-flip resonances, that is, electron spin resonance and combined resonance, (b) resonances of bound carriers, that is, internal transitions of shallow impurities and excitons, (c) polaronic coupling, that is, resonant interactions of carriers with phonons and plasmons, and (d) 1D and 2D magnetoplasmon excitations. It should be also mentioned that in 2D systems in the magnetic quantum limit, there are still unresolved issues concerning the effects of disorder and electron–electron interactions on CR (for a review, see, e.g., Petrou and McCombe, 1991; Nicholas, 1994).

It is important to note that all the early CR studies were carried out on semiconductors, not on metals. This is because of the high carrier concentrations present in metals, which preclude direct transmission spectroscopy except in the case of very thin films when the thickness is less than the depth of penetration (skin depth of the electromagnetic fields). In bulk metals, special geometries are thus required to detect CR, the most important of which is the Azbel–Kaner geometry (Azbel and Kaner, 1958). In this geometry, both the DC magnetic field $\vec{B}$ and the AC electric field $\vec{E}$ are applied parallel to the sample surface, either $\vec{B}//\vec{E}$ or $\vec{B} \perp \vec{E}$. The electrons then execute a spiral motion along B, moving in and out of the skin depth, where $\vec{E}$ is present. Thus, whenever the electron enters the skin depth, it is accelerated by the AC field, and if the phase of $\vec{E}$ is the same every time the electron enters the skin depth, then the electron can resonantly absorb energy from the AC field. The condition for resonance here is $n\omega_c = \omega$ ($n = 1$, 2, 3, ...). For more details on CR in metals, see, for example, Mavroides (1972).

Many techniques can provide information on effective masses, but none can rival CR for directness and accuracy. Effective masses can be estimated from the temperature dependence of the amplitude of the galvanomagnetic effects, that is, the Shubnikov–de Haas and de Haas–van Alphen effects. Interband magneto-optical absorption can determine the reduced mass $\mu = (1/m_e + 1/m_h)^{-1}$ of photocreated electrons and holes. Measurements of the infrared Faraday rotation effect due to free carriers can provide information on the anisotropy of elliptical equi-energy surfaces. The temperature dependence of electronic specific heat provides a good measure of the density of levels at the Fermi level, which in turn is proportional to the effective mass. Nonresonant free carrier absorption (see CARRIER LIFETIME: FREE CARRIER ABSORPTION, PHOTOCONDUCTIVITY, AND PHOTOLUMINESCENCE) can be used to estimate effective masses, but this simply represents a tail or shoulder of a CR absorption curve.

It is worth pointing out here that several different definitions of effective masses exist in the literature and care must be taken when one discusses masses. The band-edge mass, defined as in Equation 1 at band extrema (e.g., $\vec{k} = 0$ in most semiconductors), is the most important band parameter to characterize a material. The specific heat mass is directly related to the density of states at the Fermi level and is thus also called the density-of-states mass. The cyclotron mass is defined as $m_c^* = (h^2/2\pi)\partial A/\partial E$, where A is the momentum-space area enclosed by the cyclotron orbit; this definition follows naturally from calculation of ω_c in momentum space. The spectroscopic mass can be defined for any resonance peak and is identical to the cyclotron mass when the resonance is due to free carrier CR (also see Section "Data Analysis and Initial Interpretation").

The basic theory and experimental methods of cyclotron resonance are presented in this article. Basic theoretical background will first be presented (see Section "Principles of the Method"). A detailed description will then be given of the actual experimentation procedures (see Section "Practical Aspects of the Method"). Finally, typical data analysis procedures are presented (see Section "Data Analysis and Initial Interpretation").

PRINCIPLES OF THE METHOD

As described in Section "Introduction," the basic physics of CR is the interaction of electromagnetic (EM) radiation with charge carriers in a magnetic field. Here, more quantitative descriptions of this physical phenomenon will be presented, based on (1) a semiclassical model and (2) a quantum mechanical model. In analyzing CR data, appropriate combination, modification, and refinement of these basic models are necessary, depending on the experimental conditions and the material under study, in order to obtain the maximum amount of information from a given set of data.

The most commonly used method for describing the motion of charge carriers in solids perturbed by external fields is the effective mass approximation (EMA), developed by many workers in the early history of the quantum theory of solids. The beauty of this method lies in the ability to replace the effect of the lattice periodic potential on electron motion by a mass tensor, the elements of which are determined by the unperturbed band structure. In other words, instead of considering electrons in a lattice, we may consider the motion of effective mass particles, which obey simple equations of motion in the presence of external fields. Rigorous treatments and full justification of the EMA can be found in the early original papers (e.g., Wannier, 1937; Slater, 1949; Luttinger, 1951; Luttinger and Kohn, 1955).

Semiclassical Drude Description of CR

In many cases it is satisfactory to use the semiclassical Drude model (e.g., Aschcroft and Mermin, 1976) to describe the conductivity tensor of free carriers in a magnetic field (see MAGNETOTRANSPORT IN METALS AND ALLOYS). In this model, each electron is assumed to independently obey the equation of motion

$$\vec{m}^* \cdot \frac{d\vec{v}}{dt} + \vec{m}^* \cdot \frac{\vec{v}}{\tau} = e(\vec{E} + \vec{v} \times \vec{B}) \qquad (3)$$

where $\vec{m}^*$ is the effective mass tensor (see, e.g., Equation 1 for nondegenerate bands), $\vec{v}$ is the drift velocity of the electrons, τ is the scattering lifetime (which is assumed to be a constant), $\vec{E}$ is the AC electric field, and $\vec{B}$ is the DC magnetic field. The complex conductivity tensor $\vec{\sigma}$ is then defined via $\vec{J} = ne\vec{v} = \vec{\sigma} \cdot \vec{E}$, where $\vec{J}$ is the current density and n is the carrier density. Assuming that the AC field and the drift velocity have the harmonically varying form, that is, $\vec{E}(t) = \vec{E}_0 \exp(-i\omega t)$ and $\vec{v}(t) = \vec{v}_0 \exp(-i\omega t)$, one can solve Equation 3 in a straightforward manner. In particular, for cubic materials and for $\vec{B} \| \hat{z} \|$, $\vec{\sigma}$ is given by

$$\vec{\sigma} = \begin{pmatrix} \sigma_{xx} & \sigma_{xy} & 0 \\ \sigma_{yx} & \sigma_{yy} & 0 \\ 0 & 0 & \sigma_{zz} \end{pmatrix} \qquad (4a)$$

$$\sigma_{xx} = \sigma_{yy} = \sigma_0 \frac{i\omega\tau + 1}{(i\omega\tau + 1)^2 + \omega_c^2 \tau^2} \qquad (4b)$$

$$\sigma_{xy} = -\sigma_{yx} = \sigma_0 \frac{\omega_c\tau}{(i\omega\tau + 1)^2 + \omega_c^2 \tau^2} \qquad (4c)$$

$$\sigma_{zz} = \sigma_0 \frac{1}{i\omega\tau + 1} \qquad (4d)$$

$$\sigma_0 = ne\mu \frac{ne^2\tau}{m^*} \qquad (4e)$$

where μ is the carrier mobility and σ_0 is the DC conductivity.

Once we know the conductivity tensor, we can evaluate the power P absorbed by the carriers from the AC field as

$$P = \langle \vec{J}(t) \cdot \vec{E}(t) \rangle = \frac{1}{2} \text{Re}(\vec{J} \cdot \vec{E}^*) \qquad (5)$$

where $\langle \cdot \rangle$ represents the time average and $\vec{E}^*$ is the complex conjugate of $\vec{E}$. For an EM wave linearly polarized in the x direction, that is, $\vec{E} = (E_x, 0, 0)$, Equation 5 simplifies to

$$P = \frac{1}{2} \text{Re}(J_x E_x^*) = \frac{1}{2} |E_0|^2 \text{Re}(\sigma_{xx}) \qquad (6)$$

Substituting Equation 4b into Equation 6, we obtain

$$P(\omega) = \frac{1}{2} |E_0|^2 \sigma_0 \text{Re}\left\{ \frac{i\omega\tau + 1}{(i\omega\tau + 1)^2 + \omega_c^2 \tau^2} \right\}$$

$$= \frac{1}{4} |E_0|^2 \sigma_0 \left[\frac{1}{(\omega - \omega_c)^2 \tau^2 + 1} + \frac{1}{(\omega + \omega_c)^2 \tau^2 + 1} \right] \qquad (7)$$

This is plotted in Figure 1 for different values of the parameter $\omega_c\tau$. It is evident from this figure that an absorption peak occurs when $\omega = \omega_c$ and $\omega_c\tau > 1$.

Note that Equation 7 contains two resonances—one at $\omega = \omega_c$ and the other at $\omega = -\omega_c$. These two resonances correspond to the two opposite senses of circular polarization. It can be shown (see, e.g., Palik and Furdyna, 1970) that in the Faraday geometry $\vec{q} \| \vec{B} \| \hat{z}$, where $\vec{q}$ is the wavevector of the EM wave, a 3D magnetoplasma can support only two propagating EM modes represented by

$$\vec{E}_{\pm} = E_0 \frac{1}{\sqrt{2}} (\vec{e}_x \pm i\vec{e}_y) \exp[i(q_{\pm}z - \omega t)] \qquad (8)$$

where $\vec{e}_x$ and $\vec{e}_y$ are the unit vectors in the x and y directions, respectively. The dispersion relations, $q_{\pm}$ versus ω, for the two modes are obtained from

$$q_{\pm} = \frac{\omega N_{\pm}}{c} \qquad (9a)$$

$$N_{\pm}^2 = \kappa_{\pm} = \kappa_{xx} \pm i\kappa_{xy}) \qquad (9b)$$

$$\kappa_{xx} = \kappa_1 + \frac{i}{\omega\varepsilon_0} \sigma_{xx} = \kappa_1 + \frac{i\sigma_0}{\omega\varepsilon_0} \frac{i\omega\tau + 1}{(i\omega\tau + 1)^2 + \omega_c^2 \tau^2} \qquad (9c)$$

$$\kappa_{xy} = \frac{i}{\omega\varepsilon_0} \sigma_{xy} = \frac{i\sigma_0}{\omega\varepsilon_0} \frac{\omega_c\tau}{(i\omega\tau + 1)^2 + \omega_c^2 \tau^2} \qquad (9d)$$

where $N_{\pm}$ is the complex refractive index, κ_1 is the relative dielectric constant of the lattice (assumed to be
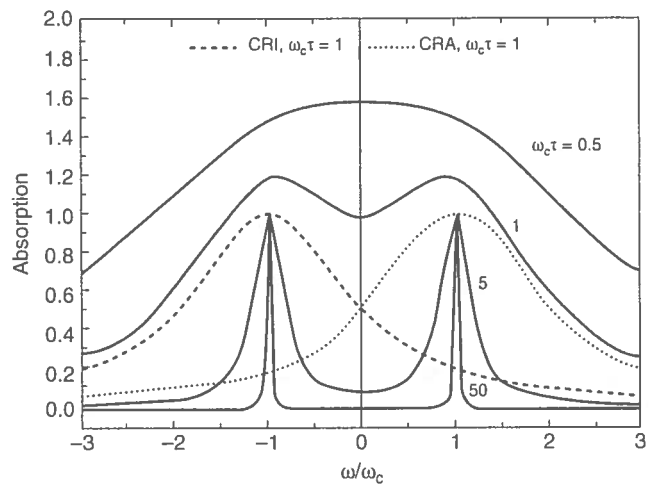
Figure 1. The CR absorption power versus ω for different values of $\omega_c\tau$. The traces are obtained from Equation 7. CR occurs at $\omega = \omega_c$ when $\omega_c\tau > 1$. The absorption is expressed in units of $|E_0|^2\sigma_0/4$.

constant in the FIR), and κ_{xx} and κ_{xy} are components of the generalized dielectric tensor $\overline{\kappa} = \kappa_l I + (i/\omega\varepsilon_0)\vec{\sigma}$, where I is the unit tensor and $\vec{\sigma}$ is the conductivity tensor (Equations 4a–4e). The positive sign corresponds to a circularly polarized FIR field, rotating in the same sense as a negatively charged particle, and is traditionally referred to as cyclotron resonance active (CRA) for electrons. Similarly, the negative sign represents the opposite sense of circular polarization, cyclotron resonance inactive (CRI) for electrons. The CRA mode for electrons is the CRI mode for holes, and *vice versa*. For linearly polarized FIR radiation, which is an equal-weight mixture of the two modes, both terms in Equation 7 contribute to the absorption curve, as represented in Figure 1.

Quantum Mechanical Description of CR

According to the EMA, if the unperturbed energy-momentum relation for the band n, $E_n(\vec{p})$, is known, then the allowed energies E of a crystalline system perturbed by a uniform DC magnetic field $\vec{B} = \vec{\nabla} \times \vec{A}$ (where $\vec{A}$ is the vector potential) are given approximately by solving the effective Schrödinger equation

$$\hat{H}F_n(\vec{r}) = \hat{E}_n(-i\hbar\vec{\nabla} + e\vec{A})F_n(\vec{r}) = EF_n(\vec{r}) \quad (10)$$

Here, the operator $\hat{E}_n(-i\hbar\vec{\nabla} + e\vec{A})$ means that we first replace the momentum $\vec{p}$ in the function $E_n(\vec{p})$ with the kinematic (or mechanical) momentum $\vec{\pi} = \vec{p} + e\vec{A}$ (see, e.g., Sakurai, 1985) and then transform it into an operator by $\vec{p} \to -i\hbar\vec{\nabla}$. The function $F_n(\vec{r})$ is a slowly varying "envelope" wavefunction; the total wavefunction $\psi(\vec{r})$ is given by a linear combination of the Bloch functions at $\vec{p} = 0$ (or the cell-periodic function), $\psi_{n0}(\vec{r})$

$$\psi(\vec{r}) = \sum_n F_n(\vec{r})\psi_{n0}(\vec{r}) \quad (11)$$

For simplicity let us consider a 2D electron in a conduction band with a parabolic and isotropic dispersion $E_n(\vec{p}) = |p|^2/2m^* = (p_x^2 + p_y^2)/2m^*$. The Hamiltonian in Equation 10 is then simply expressed as

$$\hat{H}_0 = \frac{|\vec{\pi}|^2}{2m^*} = \frac{1}{2m^*}\left(\pi_x^2 + \pi_y^2\right) \quad (12)$$

These kinematic momentum operators obey the following commutation relations:

$$[x, \pi_x] = [y, \pi_y] = i\hbar \quad (13a)$$

$$[x, \pi_y] = [y, \pi_x] = [x, y] = 0 \quad (13b)$$

$$[\pi_x, \pi_y] = -i\hbar^2/\ell^2 \quad (13c)$$

where $\ell = (\hbar/eB)^{1/2}$ is the magnetic length, which measures the spatial extent of electronic (envelope) wavefunctions in magnetic fields—the quantum mechanical counterpart of the cyclotron radius r_c. Note the noncom-

mutability between π_x and π_y (Equation 13c), in contrast to p_x and p_y in the zero magnetic field case.

We now introduce the Landau level raising and lowering operators

$$\hat{a}_\pm = \frac{\ell}{\sqrt{2\hbar}}(\pi_x \pm i\pi_y) \quad (14)$$

for which we can show that

$$[\hat{a}_-, \hat{a}_+] = 1 \quad (15a)$$

$$[\hat{H}_0, \hat{a}_\pm] = \pm\hbar\omega_c\hat{a}_\pm \quad (15b)$$

Combining Equations 13–15, we can see that $\hat{a}_\pm$ connects the state $|N\rangle$ and the states $|N\pm 1\rangle$ and that $\hat{H}_0 = \hbar\omega_c(\hat{a}_+\hat{a}_- + 1/2)$, and, hence, the eigenenergies are

$$E = \left(N + \frac{1}{2}\right)\hbar\omega_c \quad (N = 0, 1, \ldots) \quad (16)$$

These discrete energy levels are well known as Landau levels.

If we now apply a FIR field with CRA (CRI) polarization (Equation 8) to the system, then, in the electric dipole approximation, the Hamiltonian becomes

$$\hat{H} = \frac{1}{2m^*}|\vec{p} + e\vec{A} + e\vec{A}'_\pm|^2 \approx \frac{1}{2m^*}|\vec{\pi}|^2 + \frac{e}{m^*}\vec{\pi} \cdot \vec{A}'_\pm$$

$$= \hat{H}_0 + \hat{H}' \quad (17)$$

where, from Equation 8, the vector potential for the FIR field $\vec{A}'_\pm$ is given by

$$\vec{A}'_\pm = -\frac{E_0}{\sqrt{2}i\omega}(\vec{e}_x \pm i\vec{e}_y)\exp(-i\omega t) \quad (18)$$

Thus, the perturbation Hamiltonian $\hat{H}'$ is given by

$$\hat{H}' = \frac{e}{m^*}(\pi_x A'_{\pm,x} + \pi_y A'_{\pm,y})$$

$$= -\frac{eE_0}{\sqrt{2}i\omega m^*}(\pi_x \pm i\pi_y)\exp(-i\omega t)$$

$$= -\frac{e\hbar E_0}{i\omega m^*\ell}\hat{a}_\pm \exp(-i\omega t) . \quad (19)$$

We can immediately see that this perturbation, containing $\vec{a}_\pm$, connects the state $|N\rangle$ with the states $|N\pm 1\rangle$, so that a sharp absorption occurs at $\omega = \omega_c$.

PRACTICAL ASPECTS OF THE METHOD

CR spectroscopy, or the more general FIR magneto-spectroscopy, is performed in three distinct ways—laser magnetospectroscopy (LMS), Fourier transform magnetospectroscopy (FTMS), and THz time-domain

magnetospectroscopy (THz-TDMS). The former is magnetic-field-dependent spectroscopy and the latter two are wavelength-dependent spectroscopy. Generally speaking, LMS and FTMS are complementary. THz-TDMS is a recently developed method and has unique features compared to LMS and FTMS.

Narrow spectral widths and high output powers are two of the main advantages of lasers. The former makes LMS suitable for investigating spectral features that cannot be resolved by using FTMS, and the latter makes it suitable for studying absorption features in the presence of strong background absorption or reflection. It is also much easier to conduct polarization-dependent measurements by LMS than by FTMS. Moreover, LMS can be easily combined with strong pulsed magnets. Finally, with intense and short-pulse lasers such as the free electron laser (FEL; see, e.g., Brau, 1990), LMS can be extended to nonlinear and time-resolved FIR magnetospectroscopy.

On the other hand, FTMS has some significant advantages with respect to LMS. First, currently available FIR laser sources (except for FELs) can produce only discrete wavelengths, whereas FTMS uses light sources that produce continuous spectra. Second, it is needless to say that LMS can only detect spectral features that are magnetic field dependent, so that it is unable to generate zero-field spectra. Third, LMS often overlooks or distorts features that have a very weak field dependence, in which case only FTMS can give unambiguous results, the $1s \rightarrow 2p_-$ transition of shallow neutral donors being a good example (e.g., McCombe and Wagner, 1975). Finally, for studying 2D electron systems, spectroscopy at fixed filling factors, namely, at fixed magnetic fields, is sometimes crucial.

THz-TDMS has advantages over the above methods. First, this is a time-domain measurement in contrast to the above two, which are frequency-domain methods. THz-TDMS directly measures *electric field*—not the intensity—of THz radiation in the time domain, which makes this method a coherent measurement. Both real and imaginary parts of the optical constants of the sample, such as conductivities and dielectric constants, can be determined, while only one (real part of conductivity or imaginary part of dielectric constant) is determined in LMS and FTMS. Second, ultrashort THz pulses allow us to study ultrafast phenomena in subpicosecond time resolution. These are the most prominent features of THz-TDMS, which cannot be achieved by LMS or FTMS (Nuss and Orenstein, 1998; Mittleman, 2002; Sakai, 2005). In addition, THz-TDMS can study a wide range of frequencies from 0.1 THz (3 mm) to 100 THz (3 µm) with a well-defined polarization and provide strong electric fields for nonlinear optical spectroscopy.

In this section, after briefly reviewing FIR sources, these three modes of operation—LMS, FTMS, and THz-TDMS—will be described in detail. In addition, short descriptions of two other unconventional methods—cross-modulation (or photoconductivity), in which the sample itself is used as a detector, and optically detected resonance (ODR) spectroscopy, which is a recently developed, highly sensitive method—will be provided.

For the reader interested in a detailed description of FIR detectors and other FIR techniques, see, for example, Kimmitt (1970), Stewart (1970), and Chantry (1971).

Far Infrared Sources

The two "classic" sources of FIR radiation commonly used in FTMS are the globar and the Hg arc lamp. The globar consists of a rod of silicon carbide usually ~2 cm long and 0.5 cm in diameter. It is heated by electrical conduction; normally 5 A is passed through it, which raises its temperature to ~1500 K. The globar is bright at wavelengths between 2 and 40 µm, but beyond 40 µm its emissivity falls slowly, although it is still sufficient for spectroscopy up to ~100 µm. The mercury lamp has higher emissivity than the globar at wavelengths longer than 100 µm. It is normally termed a "high-pressure" arc, although the actual pressure is only 1–2 atm. (Low-pressure gaseous discharges are not useful here because they emit discrete line spectra.) It is contained in a fused quartz inner envelope. At the shorter wavelengths of the FIR, quartz is opaque, but it becomes very hot and emits thermal radiation. At the longer wavelengths, radiation from the mercury plasma is transmitted by the quartz and replaces the thermal radiation. Originally used by Rubens and von Baeyer (1911), the mercury arc lamp is still the most widely employed source in the FIR.

Four types of laser sources currently available to FIR spectroscopists are molecular gas lasers, the FEL, the p-type germanium laser, and the quantum cascade laser. The most frequently used among these are the hundreds of laser lines available from a large number of molecular gases. The low-pressure gas consisting of HCN, H_2O, D_2O, CH_3OH, CH_3CN, etc., flows through a glass or metal tube, where population inversion is achieved either through a high-voltage discharge or by optical excitation with a CO_2 laser. Output powers range from a few microwatts to several hundred milliwatts, depending on the line, gas pressure, pumping power, and whether continuous or pulsed excitation is used. The FEL, first operated in 1977, is an unusual laser source that converts the kinetic energy of free electrons to EM radiation. It is tunable in a wide range of frequencies, from millimeter to ultraviolet. An FEL consists of an electron gun, an accelerator, an optical cavity, and a periodic array of magnets called an undulator or wiggler. The wavelength of the output optical beam is determined by (1) the kinetic energy of the incident electrons, (2) the spatial period of the wiggler, and (3) the strength of the wiggler magnets, all of which are continuously tunable. With FEL's enormously high peak powers (up to ~1 GW) and short pulse widths (down to ~200 fs), a new class of nonequilibrium phenomena is currently being explored in the FIR. The p-Ge laser is a tunable solid-state FIR laser (for a review, see Gornik, 1991; Pidgeon, 1994). Its operation relies on the fact that streaming holes in the valence band in crossed strong electric and magnetic fields can result in an inverted hot-carrier distribution. Two different lasing processes, employing light hole–light hole and light hole–heavy hole transitions, respectively, have been identified (the former is the first

realization of a CR laser). The lasing wavelength is continuously tunable, by adjusting the electric and magnetic fields. Lasing in a wide spectral range ($75–500\,\mu m$) with powers up to almost 1 W has been reported. The quantum cascade laser (Capasso et al., 2002) was initially developed for the mid-infrared range, but its wavelength range has been recently extended to the far infrared/THz (Williams, 2007), opening up new possibilities. Its compactness is ideal for experimental setups for which space is limited, and its spectral and intensity stabilities have been shown to be adequate for CR studies (Larrabee et al., 2004).

The remarkable advances in high-speed optoelectronic and NIR/visible femtosecond laser technology have enabled generation and detection of ultrashort pulses of broadband coherent FIR radiation (more frequently referred to as THz radiation or "T rays" in this context), which gave birth to THz-TDMS. There are several generation methods (Mittleman, 2002; Sakai, 2005) for T-rays. Hertzian dipole radiation from a transient photocurrent induced by femtosecond laser pulses in a photoconductive (PC) antenna is one of the most widely used methods. Low-temperature-grown GaAs is frequently used as the substrate of the PC antenna due to its excellent properties. The other common method is an optical rectification of femtosecond laser pulses using nonlinear crystals (e.g., ZnTe and GaP). These methods can typically provide THz radiation pulses containing frequencies from ~0.1 to $\sim3\,THz$. Recent advances in THz air photonics, which uses air (nitrogen) or several types of gases (e.g., xenon, alkanes, etc.) as emitters and detectors, provide broader bandwidths up to $\sim30\,THz$ (Ho et al., 2010). For higher frequencies up to $100\,THz$, NIR/visible laser pulse as short as $10\,fs$ is used for the optical rectification in GaSe and $LiIO_3$ crystal (Huber et al., 2008). Owing to the recent breakthroughs in the development of Cherenkov-type optical rectification in lithium niobate crystals, strong THz electric fields as high as $100\,kV/cm$ can be generated and used for the nonlinear THz spectroscopy (Hebling et al., 2010).

Fourier Transform FIR Magnetospectroscopy

A Fourier transform spectrometer is essentially a Michelson-type two-beam interferometer, the basic components of which are collimating optics, a fixed mirror, a beam splitter, and a movable mirror. The basic operation principle can be stated as follows. IR radiation emitted from the light source is divided by the beam splitter into two beams with approximately the same intensity. One of the beams reaches the fixed mirror, and the other reaches the movable mirror. The two beams bounce back from the two mirrors and recombine at the beam splitter. When the movable mirror is at the zero-path-difference (ZPD) position, the output of the light intensity becomes maximum, since the two beams constructively interface at all wavelengths. When the path difference, x, measured from the ZPD position is varied, an interference pattern as a function of x, called an interferogram, is obtained, which is the Fourier transform of the spectrum of the, light passing through the interferometer. Hence, by taking the inverse Fourier transform of the interferogram using a computer, one obtains the spectrum.

Two different types of FT spectrometers exist: (1) "slow-scan" (or step-scan) and (2) "fast-scan" spectrometers. In a slow-scan FT spectrometer, a stepping motor drives the movable mirror. A computer controls the step size in multiples of the fundamental step size, the dwell time at each mirror position, and the total number of steps. The product of the step size and the number of steps determines the total path difference, and, hence, the spectral resolution. A mechanical chopper (see Fig. 2) usually chops the FIR beam. The AC signal at this frequency from the detector is fed into a lock-in amplifier and the reference signal from the chopper into the reference input of the lock-in amplifier. The data acquisition occurs at each movable mirror position, and, thus, an interferogram is constructed as the magnitude of the output versus the position of the movable mirror. Computer Fourier analysis with a fast Fourier transform (FFT) algorithm converts the interferogram into an intensity versus frequency distribution—the spectrum.

Rapid-scan FT spectrometers operate quite differently, although the basic principles are the same. The movable mirror of a rapid-scan FT machine is driven at a constant velocity. Instead of using a mechanical chopper, the constant velocity of the mirror produces a sinusoidal intensity variation with a unique frequency for each spectral element ω. The modulation frequency is given by $\vartheta = 2V\omega$, where V is the velocity of the mirror. High precision of parallel alignment between the two mirrors and the constant velocity of the moving mirror is provided *in situ* by a dynamic feedback controlling system. The signal sampling takes place at equally spaced mirror displacements and is determined by the fringes of an He–Ne laser reference.

A slow-scan FTMS system for transmission CR studies is schematically shown in Figure 2. FIR radiation generated by an Hg arc lamp inside the spectrometer is coupled out by a Cassegrain output mirror and guided through a 3/4-in. ("oversized") brass light pipe to a 45° mirror. The beam reflected by the mirror is then directed down and passes through a white polyethylene window into a sample probe, which consists of a stainless steel light pipe, a sample holder/heater/temperature sensor complex, metallic light cones, and a detector. The probe is sealed by the white polyethylene window and a stainless steel vacuum jacket, and inserted into a superconducting magnet cryostat. The beam is focused by a condensing cone onto the sample located at the end of the light cone at the center of the field. A black polyethylene filter is placed in front of the sample in order to filter out the high-frequency part ($\geq500\,cm^{-1}$) of the radiation from the light source. The FIR light transmitted through the sample is further guided by light pipe/light cone optics into a detector, which is placed at the bottom of the light pipe system, far away from the center of the magnet. If a cancellation coil is available, the detector is placed at the center of the cancellation coil where $B=0$. The sample and detector are cooled by helium exchange gas contained in the vacuum jacket of the probe.
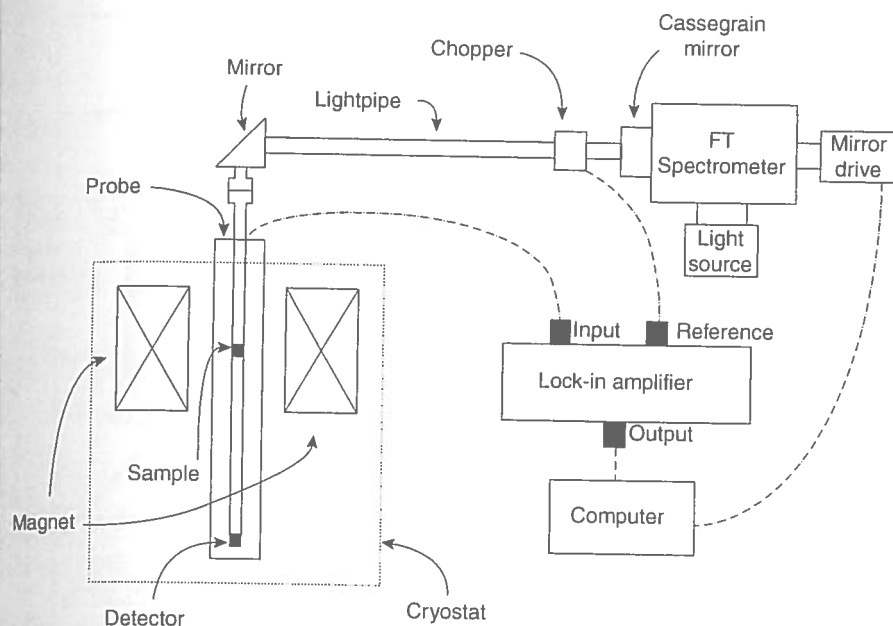
Figure 2. Schematic diagram of an experimental setup for CR studies with a (step-scan) Fourier transform spectrometer.

Figure 3a and b shows a typical interferogram and spectrum, respectively. The spectrum obtained contains not only the spectral response (transmittance in this case) of the sample but also the spectral response of combined effects of any absorption, filtering, and reflection when the light travels from the source to the detector, in addition to the output intensity spectrum of the radiation source. Therefore, in most experimental

(a) Sample = InAs/Al$_{0.1}$Ga$_{0.9}$Sb QW
Detector = SH
Points = 256
Step size = 10 μm
No. of passes = 6
Magnetic field = 5 T

(b) Sample = InAs/Al$_{0.1}$Ga$_{0.9}$Sb QW
Detector = SH
Points = 256
Step size = 10 μm
No. of passes = 6
Magnetic field = 5 T
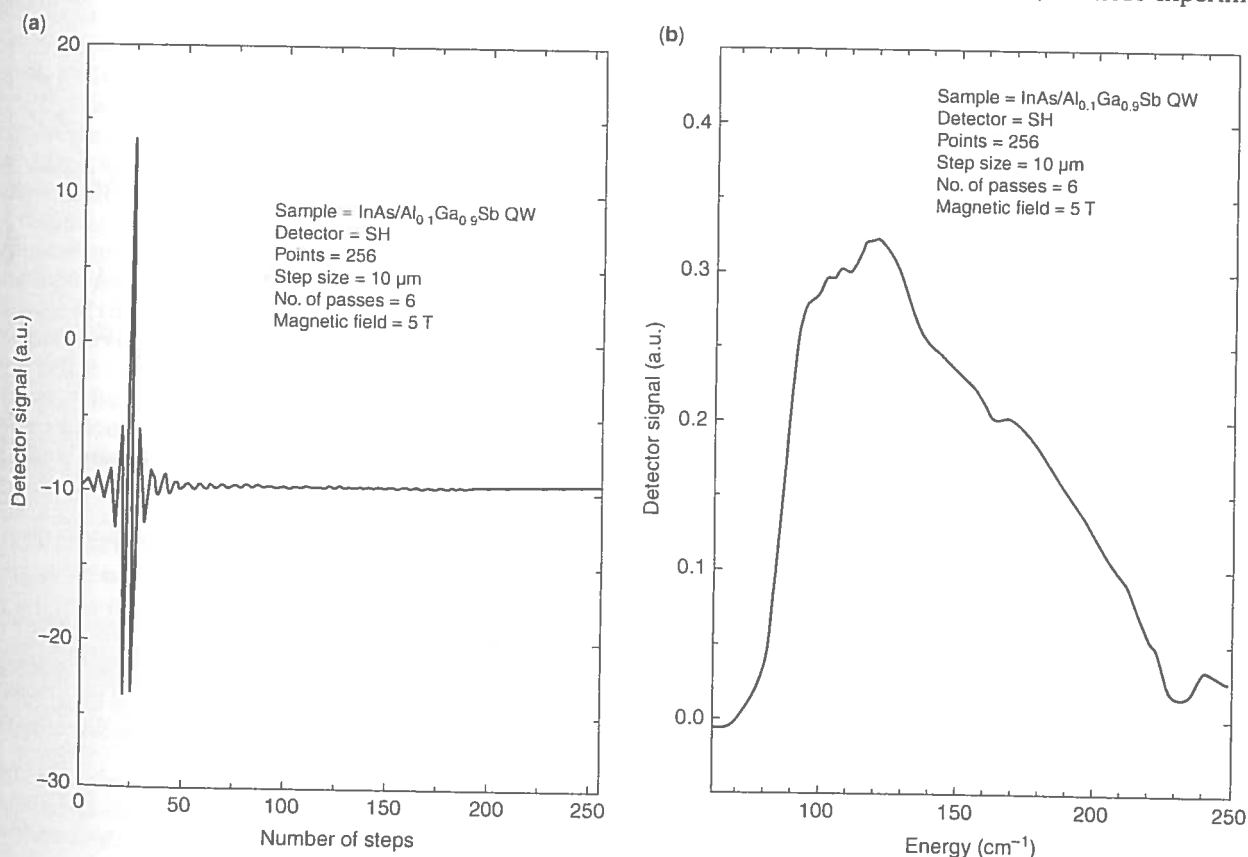
Figure 3. (a) An interferogram obtained with the FTMS setup shown in Figure 2. (b) Spectrum obtained after Fourier transforming the interferogram in (a). This spectrum contains the output intensity spectrum of the Hg arc lamp, the spectral response of all the components between the source and the detector (filters, light pipes, light cones, etc.), the responsivity spectrum of the detector (Ge:Ge extrinsic photoconductor), as well as the transmission spectrum of the sample.

situations, spectra such as those obtained in Figure 3b are ratioed to an appropriate background spectrum taken under a different condition such as a different magnetic field, temperature, optical pumping intensity, or some other parameter that would only change the transmittance of the sample. In CR studies, spectra are usually ratioed to a zero magnetic field spectrum. In this way all the unwanted field-insensitive spectral structures are canceled out.

Laser FIR Magnetospectroscopy

LMS is generally easier to carry out than FTMS, although the experimental setup is almost identical to that of FTMS (the only difference is that the FT spectrometer is replaced by a laser in Fig. 2). This is partly because of the high power available from lasers compared with conventional radiation sources employed in FTMS, and also because mathematical treatments of the recorded data are not required. The data acquisition simply consists of monitoring an output signal from the detector that is proportional to the amount of FIR light transmitted by the sample while the magnetic field is swept. The signal changes with magnetic field, decreasing resonantly and showing minima at resonant magnetic fields (see Fig. 4). Only magnetic-field-dependent features can thus be observed. If the laser output is stable while the field is being swept, no ratioing is necessary.

A very important feature of LMS is that it can easily incorporate pulsed magnets, thus allowing observations of CR at very high magnetic fields (see Miura, 1984; Kono and Miura, 2006). Pulsed magnetic fields up to 40–60 T with millisecond pulse durations can be routinely produced at various laboratories. Stronger magnetic fields in the megagauss (1 MG = 100 T) range can be also generated by special destructive methods (see, e.g., Herlach, 1984) at some institutes. These strong fields have been used to explore new physics in the ultraquantum limit (see, e.g., Herlach, 1984; Miura, 1984) as well as to observe CR in wide-gap, heavy-mass, and low-mobility materials unmeasurable by other techniques (see, e.g., Kono et al., 1993). The cyclotron energy of electrons in megagauss fields can exceed other characteristic energies in solids such as binding energies of impurities and exciton–optical phonon energies, plasma energies, and even the fundamental bandgap in some materials, causing strong modifications in CR spectra.

An example of megagauss CR is shown in Figure 4. Here, the recorded traces of the magnetic field pulse and the transmitted radiation from an n-type silicon carbide sample are plotted in Figure 4a. The transmitted signal is then plotted as a function of magnetic field in Figure 4b. The 36-µm line from a water-cooled H_2O vapor pulse laser and a Ge:Cu impurity photoconductive detector are used. The magnetic field is generated by a destructive single-turn coil method (see, e.g., Herlach, 1984), in which one shot of large current (~2.5 MA) from a fast capacitor bank (100 kJ, 40 kV) is passed through a thin single-turn copper coil. Although the coil is destroyed during the shot due to the EM force and the Joule heat, the sample can survive a number of such shots, so that
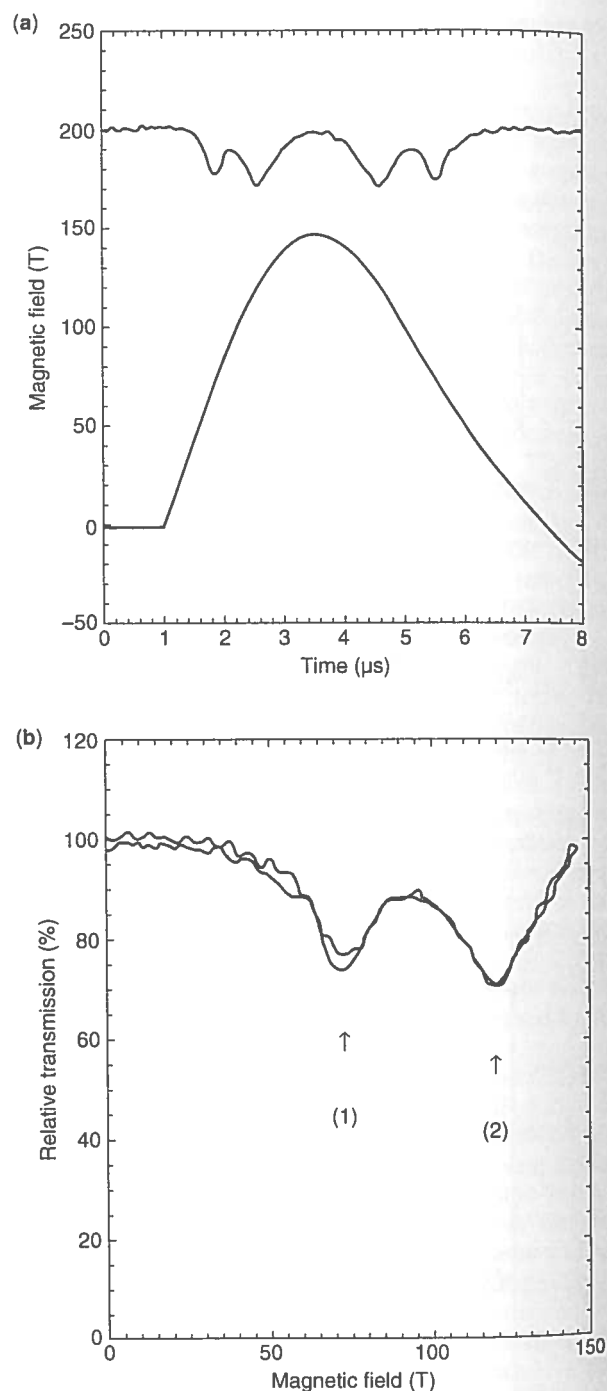
Figure 4. Example of CR with a laser in very high pulsed magnetic fields. (a) FIR transmission and magnetic field as functions of time. (b) Replot of the transmission signal as a function of magnetic field where the two traces arise from the rising and falling portions of the field strength shown in (a). Data obtained for n-type 3C-SiC.

repeated measurements can be made on the same sample. The resonance absorption is observed twice in one pulse, in the rising and falling slopes of the magnetic field, as seen in Figure 4. It should be noted that the coincidence of the two traces (Fig. 4b) confirms a sufficiently fast response of the detector system.
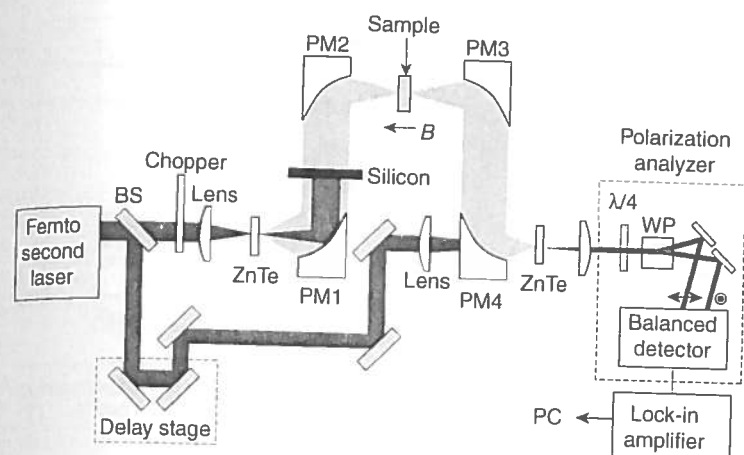
Figure 5. Experimental setup of THz-TDMS. A silicon plate is used to block the residual laser pulse after the emitter ZnTe. $\lambda/4$, quarter wave plate; WP, Wollaston prism.

THz Time-domain Magnetospectroscopy

THz-TDMS requires a rather complicated optical system compared to LMS and FTMS. Figure 5 shows a typical experimental setup utilizing ZnTe as an emitter and detector. The NIR/visible femtosecond laser beam is split into two by a beam splitter (BS). The majority of the pulse energy is directed into one of these two beams and is used to generate THz pulses via optical rectification. THz pulses are focused to a frequency-independent beam waist at the sample at the center of the superconducting magnet by the first and second parabolic mirrors (PM1 and PM2), and the transmitted THz pulses are again focused to a frequency-independent waist at the ZnTe detector crystal by the third and fourth parabolic mirrors (PM3 and PM4).

Direct electric field detection is accomplished using electro-optic sampling. This technique resolves the amplitude and phase of the THz field in the time domain using a portion of the NIR/visible laser pulse. The birefringence of the ZnTe crystal induced by the THz electric field rotates the linear polarization of the time-delayed probe pulse, which is measured using a polarization analyzer. The rotation angle and the direction of the rotation correspond to the THz electric field amplitude and sign, respectively, at the value of the THz-probe pulse delay. By scanning the arrival time of the probe pulse using a delay stage, the whole electric field waveform is recorded as a function of time, as shown in Figure 6. In most cases, the laser pulse generating the THz pulse is modulated by an optical chopper (low frequency $\sim$1 kHz) or an acousto-optic modulator (high frequency $\sim$50 MHz) for lock-in detection. By Fourier transforming the time-domain data, the power spectrum and the phase in the frequency domain can be obtained (Fig. 7a–c).

An example of time-domain CR in a high-mobility two-dimensional electron gas (2DEG) is shown in Figure 6 (Wang et al., 2007, 2010). Small-amplitude coherent oscillations are seen in the waveform in the presence of a magnetic field, which become clear by subtracting the 0 T waveform. The oscillations are due to CR, and the frequency matches the CR frequency. In the frequency domain, one can see a clear dip (absorption) and disper-

sion at the CR frequency in the amplitude ratio and phase difference between the waveform data with and that without a magnetic field, respectively (Fig. 7b and c). Through data analysis (see Section "Data Analysis and Initial Interpretation"), both real and imaginary parts of the conductivity can be experimentally determined (Fig. 7d). Solid curves (theory) in Figure 7d are fitting by Equation 4b.

Cross-Modulation (or Photoconductivity)

It is well known that the energy transferred from EM radiation to an electron system due to CR absorption induces significant heating in the system (free carrier or Drude heating). This type of heating in turn induces a change in the conductivity tensor (e.g., an increase in $1/\tau$ or m), which causes (third-order) optical nonlinearity and modulation at other frequencies, allowing an observation of CR at a second frequency. Most conveniently, the DC conductivity $\sigma(\omega = 0)$ shows a pronounced
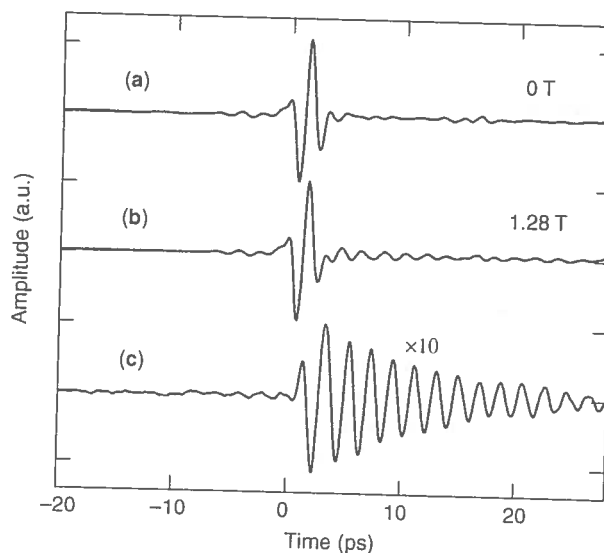

Figure 6. THz waveforms transmitted through a high-mobility 2DEG in GaAs single quantum well at (a) 0 T and (b) 1.28 T at 2 K. The cyclotron oscillations induced by the magnetic field (c) are isolated by subtracting (a) from (b) (Wang et al., 2007).
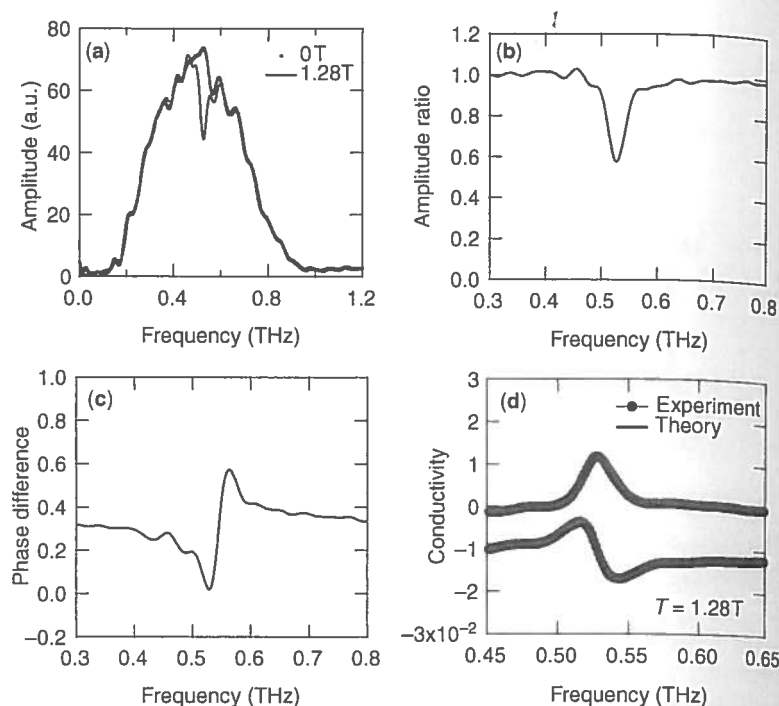
Figure 7. (a) Amplitude of the Fourier transformed electric fields at 0 and 1.28 T. (b) Magnitude of the complex transmission coefficient at 1.28 T. (c) Phase of the transmission coefficient. (d) Real (σ'_{xx}) and imaginary (σ''_{xx}) parts of the magnetoconductivity tensor element σ_{xx} at 1.28 T. The σ''_{xx} trace is vertically offset (Wang et al., 2007).

change at a resonant magnetic field. This effect is known as cross-modulation or CR-induced photoconductivity, and has been described as a very sensitive technique to detect CR (Zeiger et al., 1959; Lax and Mavroides, 1960). The beauty of this method is that the sample acts as its own detector, so that there is no detector-related noise. The disadvantage is that the detection mechanism(s) is not well understood, so that quantitative lineshape analysis is difficult, unlike direct absorption. Either a decrease or increase in conductivity is observed, depending on a number of experimental conditions. Although many suggestions concerning the underlying mechanism(s) have been proposed, a complete understanding has been elusive.

Contrary to the situation of CR, which is a free carrier resonance, the mechanism of photoconductivity due to bound carrier resonances is much more clearly understood (see CARRIER LIFETIME: FREE CARRIER ABSORPTION PHOTO- CONDUCTIVITY, AND PHOTOLUMINESCENCE). For example, a resonant absorption occurs due to the 1s to 2p hydrogenic impurity transition in zero magnetic field in GaAs. Although the 2p state is below the continuum, an electron in the 2p state can be thermally excited into the conduction band, increasing conductivity (photothermal ionization). Other p-like excited states also can be studied in this manner, and these states evolve with increasing magnetic fields. As a result, one can map out the hydrogenic spectrum of the GaAs impurities simply by studying the photoconductivity of the sample. Since this is a null technique (i.e., there is photoresponse only at resonances), it is much more sensitive than transmission studies.

Optically Detected Resonance Spectroscopy

Recently, a great deal of development work has centered on a new type of detection scheme, ODR spec-

troscopy in the FIR. This novel technique possesses several significant advantages over conventional CR methods, stimulating considerable interest among workers in the community. With this technique, FIR resonances are detected through the change in the intensity of photoluminescence (PL; see CARRIER LIFE- TIME: FREE CARRIER ABSORPTION, PHOTOCONDUCTIVITY, AND PHOTOLUMINESCENCE) while the magnetic field is swept, rather than measuring FIR absorption directly. This technique, originally developed for the microwave region, was extended to the FIR by Wright et al. (1990) in studies of epitaxial GaAs, and subsequently by others. Remarkable sensitivity in comparison with conventional FIR methods has been demonstrated in studies of CR (e.g., Ahmed et al., 1992), impurity transitions (Michels et al., 1994; Kono et al., 1995), and internal transitions in excitons (Cerne et al., 1996; Salib et al., 1996). Since carriers are optically created, ODR enables detection of CR in "clean" systems with no intentional doping, with increased scattering time, and in materials for which doping is difficult. Furthermore, with ODR it is possible to select a specific PL feature in the spectrum, among various band-edge features, as the detection "channel." It is then possible to use the specificity of the FIR spectrum to obtain information about recombination mechanisms and the interactions that give rise to the various lines.

Figure 8a is a schematic of the experimental appara- tus used for an ODR study (Kono et al., 1995). The sample is mounted in the Faraday geometry in an FIR light pipe at the center of a 9-T superconducting magnet cooled to 4.2 K. PL is excited with the 632.8 nm line of an He–Ne laser via a 600-μm-diameter optical fiber. The signals are collected with a second 600-μm fiber, and analyzed with 0.25-m single-grating spectrometer/Si diode detector combination. A CO_2-pumped FIR laser
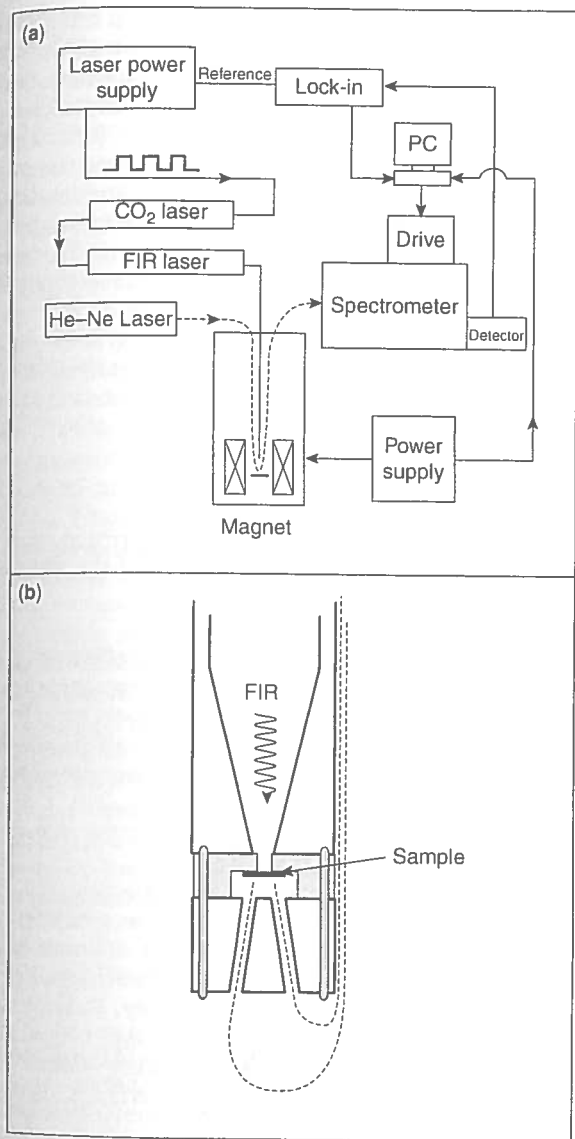
Figure 8. **(a)** Schematic diagram of an experimental setup for ODR spectroscopy. **(b)** Diagram of the FIR light cone, sample, and optical fiber arrangement used.

is used to generate FIR radiation. The FIR laser power supply is chopped with the lock-in amplifier referenced to this chopped signal. A computer is used to simultaneously record the magnetic field values and the detected changes in the PL, and to step the monochromator to follow the center of the desired PL peak as it shifts with the magnetic field. Two scans of the change in PL intensity as a function of magnetic field (ODR signal) for an FIR laser line of 118.8 μm are presented in Figure 9. The upper trace shows a positive change (i.e., increase) in the intensity of the free exciton PL from a well-center-doped GaAs quantum well, whereas the lower trace shows a negative change (i.e., decrease) in the intensity of the bound exciton luminescence, demonstrating spectral specificity. For both scans, four different FIR resonances are clearly seen with an excellent signal-to-noise ratio (the sharp feature near 6 T is the electron CR, and the other features are donor-related features).
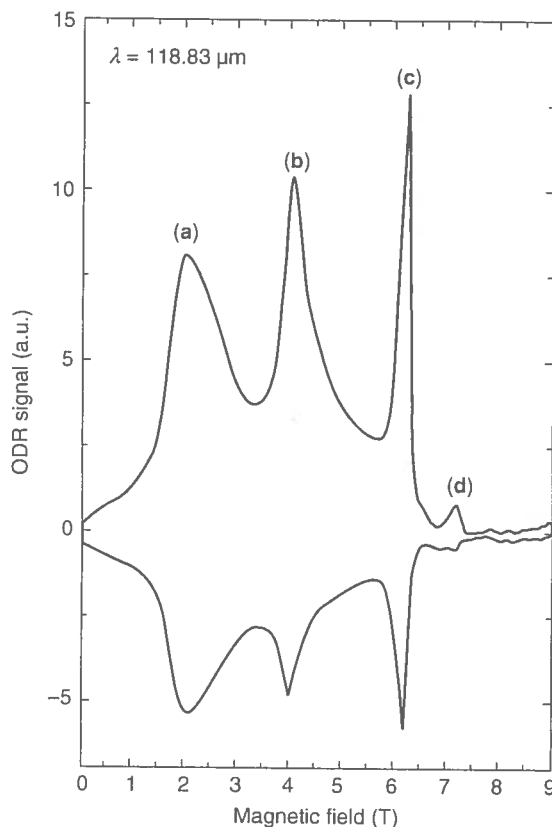
Figure 9. Two ODR spectra for a well-center-doped GaAs quantum well at an FIR wavelength of 118.8 μm. The upper trace shows a positive change in the intensity of the free exciton PL, whereas the lower trace shows a negative change in the intensity of the bound exciton luminescence, demonstrating the spectral specificity of ODR signals.

DATA ANALYSIS AND INITIAL INTERPRETATION

After minimizing noise to get as clean a spectrum as possible, and making sure that the spectrum is free from any artifacts and multiple-reflection interference effects, one can analyze resonance "positions" (i.e., magnetic fields in LMS and frequencies in FTMS or THz-TDMS). For each resonance feature, an effective mass m^* in units of m_0 (free electron mass in vacuum) can be obtained in different unit systems as follows:

$$\frac{m^*}{m_0} = \frac{eB}{m_0 \omega} = \frac{0.1158 \cdot B\,[T]}{\hbar\omega\,[meV]} = \frac{0.9337 \cdot B\,[T]}{\tilde{\nu}\,[cm^{-1}]}$$
$$= \frac{27.99 \cdot B\,[T]}{f\,[GHz]} = 93.37 \cdot B\,[T] \cdot \lambda\,[m] \tag{20}$$

Note that one can obtain an effective mass (a spectroscopic mass) for any resonance. For example, for the resonances (1) and (2) for SiC in Figure 4b one can obtain $m_1 = 0.247 m_0$ and $m_2 = 0.406 m_0$, and for the resonances (a)–(d) for doped GaAs quantum wells in Figure 9 one can obtain $m_a = 0.023 m_0$, $m_b = 0.044 m_0$, $m_c = 0.069 m_0$, and $m_d = 0.079 m_0$, irrespective of their origins. However, the spectroscopic mass is identical to the cyclotron mass only when the feature is due to free carrier CR; bound

carrier resonances, such as the donor-related features in Figure 9, have different spectroscopic masses at different frequencies/fields. Hence, one needs to know which spectroscopic feature(s) arises from free carrier CR. This can be found by two methods: temperature dependence and magnetic field (or frequency) dependence.

Examining the temperature dependence of a spectral feature is the easiest way to check the origin of the feature. As a rule of thumb, features associated with bound carriers increase in intensity with decreasing temperature at the expense of free carrier resonances. This is because in bulk semiconductors with doping level below the Mott condition, free carriers freeze out onto impurities, leaving no electrical conductivity at the lowest temperature. Thus, free carrier CR grows with increasing temperature, but it broadens with the resulting increase of carrier scattering.

A more stringent test of whether a particular feature originates from CR is the response of its frequency versus magnetic field. In the case of LMS, one can take data only at discrete frequencies, but in the case of FTMS or THz-TDMS one can generate a continuous relationship between frequency and magnetic field. This is one of the advantages of FTMS and THz-TDMS over LMS as discussed earlier. Therefore, LMS is usually performed to study, at a fixed wavelength with a higher resolution than FTMS and with circular polarizers, if necessary, those spectral features whose magnetic field dependence is already known by FTMS. The resonance frequency versus magnetic field thus obtained for CR should show a straight line passing through the origin, if the nonparabolicity of the material is negligible and there are no localization effects (e.g., Nicholas, 1994). The slope of this straight line then provides the spectroscopic mass, which is constant and identical to the cyclotron mass and is also equal to the band-edge mass in this idealized situation. In the case of a nonparabolic band, the cyclotron mass gradually increases with magnetic field. This means that the slope versus magnetic field for CR becomes smaller (i.e., the line bends down) with increasing magnetic field.

Impurity-related lines, on the other hand, extrapolate to *finite* frequencies at zero magnetic field, corresponding to the zero-field binding energies of impurities. Different transitions have different slopes versus B, but all transitions originating from the same impurity atoms converge to an approximately common intersect at zero field. The most dominant donor-related line, the 1s to 2p transition, is sometimes called impurity-shifted CR (ICR). This is because its slope versus B becomes nearly equal to that of free electron CR in the high-field limit, that is, $\hbar\omega_c \gg R_y^*$, where R_y^* is the binding energy of the impurity at zero field (McCombe and Wagner, 1975).

In many cases, multiple CR lines are observed in one spectrum (see, e.g., Dresselhaus et al., 1955; Otsuka, 1991; Petrou and McCombe, 1991; Nicholas, 1994). This generally indicates the existence of multiple types of carriers with different masses. Possible origins include: multivalley splitting in the conduction band, light holes and heavy holes in the valence band, splitting due to resonant electron–phonon coupling, nonparabolicity-induced spin splitting, Landau level splitting (see THEORY OF MAGNETIC PHASE TRANSITIONS), and population of two subbands in a quantum well. Explanation of each of these phenomena would be beyond the scope of this article.

As discussed in Section "Introduction," CR linewidth is a sensitive probe for studying carrier scattering phenomena. In general, the linewidth of a CR line is related to the scattering lifetime, and the integrated absorption intensity of a CR line is related to the density of carriers participating in CR. Thus, if the carrier density is constant, the product of absorption linewidth and depth is constant, even though the width and depth are not individually constant. More quantitatively, if the observed lineshape is well fitted by a Lorentzian, in the small absorption and reflection approximation it may be compared with

$$\frac{T(\omega,B)}{T(\omega,0)} = 1 - A(\omega,B) = 1 - \frac{1}{2}\frac{dne^2\tau}{c\varepsilon_0\kappa_l^{1/2}m^*}\frac{1}{1+(\omega-\omega_c)^2\tau^2}$$

(21)

where T is the intensity transmission coefficient, A is the corresponding absorption, d is the sample thickness, c is the speed of light, and the other symbols have been defined earlier. The half-width at half-maximum (HWHM) is thus equal to $1/\tau$. The peak absorption depth gives an estimate of the carrier density. For a more detailed and complete description on carrier transport studies using CR, see Otsuka (1991).

The detected signal in a THz-TDMS experiment is the electric field of the transmitted waveform as a function of time and magnetic field, $E(t, B)$. This is different from both FTMS and LMS, where the detected signal is a frequency- and field-dependent quantity. Calculating the frequency spectra, $E(\omega, B)$, in THz-TDMS is typically done using FFT algorithms; these are widely available in most mathematical packages (e.g., MATLAB, Maple, Igor, Mathematica, Microsoft Excel).

The frequency resolution of the acquired transmission coefficient is determined by the temporal window, W, of the acquired time-domain waveform. A narrow spectral feature (as in Equation 21) would result in a time-domain feature with a temporal lifetime, τ_d, inversely proportional to the frequency linewidth, $\delta\nu$. If the acquisition window is smaller than the temporal lifetime ($W < \tau_d$), the recovered frequency linewidth, $\delta\nu$, is limited by the measurement apparatus and does not correctly determine the material parameter. The minimum temporal window should be much longer than the decay lifetime expected for the sample to ensure multiple frequency samples within the spectral feature of interest.

The frequency window, $\Delta\nu$, is likewise determined by the acquisition of the THz waveform in the time domain; in this case, the highest frequency is limited by the inverse of the temporal step size, $\delta\tau$. High frequency content in the THz waveform will necessarily appear as rapidly changing features in the time domain. The Whittaker–Shannon sampling theorem requires a minimum sampling interval of $\delta t \le {}^1/_2\Delta\nu^{-1}$ to ensure proper

recovery of the actual waveform from the sampled data (Goodman, 1996).

Phase-sensitive detection is a critical difference between THz-TDMS and FTIR techniques. In FTIR, the phase is typically recovered by performing a broadband measurement of the sample amplitude transmission coefficient, $T(\omega, B)$, and using the well-known Kramers–Kronig relations (Born and Wolf, 1999) to calculate the corresponding phase, $\phi(\omega, B)$. Because the detection schemes described in the prior section measure the electric field (both amplitude and phase) of the transmitted THz pulses directly, the calculated FFT of the waveforms is the full complex frequency spectrum (amplitude and phase). The amplitude and phase of the transmission coefficient result directly from the THz transmission measurement using THz-TDMS, as described in the prior section (see the discussion in Section "Practical Aspects of the Method").

Because the detection scheme is phase sensitive, elements of the complex magnetoconductivity tensor of the sample can be directly recovered. If the input polarization is linearly polarized along the x direction (as is the case in many ZnTe-based systems), the transmitted THz field is, in general, elliptically polarized. The component of the transmitted polarization parallel to the input polarization ($E_{T,x}$) is determined by the on-diagonal element of the conductivity tensor, while the cross-polarized component ($E_{T,y}$) is dependent on the off-diagonal element of the complex magnetoconductivity tensor. In the thin-film approximation, the complex field transmission coefficient, $t(\omega, B)$, is given by

$$t(\omega, B) = \frac{E(\omega, B)}{E(\omega, 0)} = \frac{2n}{2n + Z_0 \sigma(\omega, B)} \qquad (22)$$

where $Z_0 = 377\,\Omega$, n is the refractive index of the sample, and $\sigma(\omega, B)$ is the complex magnetoconductivity tensor (Nuss and Orenstein, 1998). The determination of the full complex transmission coefficient (both amplitude and phase) permits the direct recovery of the relevant complex magnetoconductivity element.

SAMPLE PREPARATION

Cyclotron resonance does not require any complicated sample preparation unless it is combined with other experimental techniques. The minimum sample size required depends on the design of the FIR optics used, that is, how tightly the FIR beam can be focused onto the sample. Highly absorptive samples and samples with high carrier concentrations need to be polished down so that they are thin enough for transmission studies. In LMS and FTMS, wedging the sample substrates 2–3° is necessary to avoid multiple-reflection interference effects. Choosing the right sample is crucial for the success of a CR study. Samples with the highest possible carrier mobility are always preferable, if available. The DC mobility and density (see CONDUCTIVITY MEASUREMENT) can provide a rough estimate for the CR lineshape expected.

PROBLEMS

Generally speaking, the FIR (or THz) frequency regime, where CR is usually observed, is a difficult spectral range in which to carry out sophisticated spectroscopy. This range lies in the so-called "technology gap" existing between electronics ($\leq 100\,$GHz) and optical ($\geq 10\,$THz) frequencies. The well-developed NIR/visible technology does not extend to this range; sources are dimmer and detectors are less sensitive. In addition, because of the lack of efficient nonlinear crystals, there exist no amplitude or phase modulators in the FIR, except for simple mechanical choppers. Therefore, in many experiments, one deals with small signals having large background noise. In steady-state experiments with a step-scan FT spectrometer, lock-in techniques are always preferable. Modulating a property of the sample that only changes the size of the signal of interest—for example, modulating the carrier density with tunable gate electrodes—has proven to be a very efficient way to detect small signals. The cross-modulation (or photoconductivity) technique is also frequently used to detect small signals since it is a very sensitive method, as discussed earlier.

Aside from this signal-to-noise problem inherent in the FIR, there are some additional problems that CR spectroscopists might encounter. A problem particularly important in bulk semiconductors is the carrier freeze-out effect mentioned earlier. In most semiconductors, low-temperature FIR magnetospectra are dominated by impurity transitions. At high temperatures, free carriers are liberated from the impurities, but at the same time CR often becomes too broad to be observed because of the increased scattering rate. Thus, one has to be careful in choosing the right temperature range to study CR. In very pure semiconductors, the only way to get any CR signal is by optical pumping. In Si and Ge, whose carrier lifetimes are very long (approximately milliseconds in high-quality samples), one can create a large number of carriers sufficient for steady-state FIR absorption spectroscopy. In direct-gap semiconductors such as GaAs, carrier lifetimes are very short ($\leq 1\,$ns), so that it is nearly impossible to create enough carriers for steady-state FIR experiments, although short-pulse NIR–FIR two-color spectroscopy with an FEL is able to capture transient FIR absorption by photocreated non-equilibrium carriers. In low-dimensional semiconductor systems, so-called modulation doping is possible, where carriers can be spatially separated from their parent impurities so that they do not freeze out even at the lowest temperature.

The use of a strong magnet introduces a new class of problems. As we have seen above, in all CR studies, in the form of FTMS, THz-TDMS, or LMS, the transmission through the sample at finite magnetic field is compared with the transmission at zero magnetic field. The success of this ratioing relies on the assumption that it is only the sample that changes transmissivity with magnetic field. If anything else in the system changes some property with magnetic field, this method fails. Therefore, great care must be taken in order to make sure that no optical

components have magnetic-field-dependent characteristics, that the FIR source and detector are not affected by the magnetic field, and that no component moves with magnetic field.

ACKNOWLEDGMENTS

BIBLIOGRAPHY

"Cyclotron Resonance" *in Characterization of Materials*, 1st ed., Vol. 2, pp. 805–816, by J. Kono, Rice University, Houston, Texas; Published online: October 15, 2002; DOI: 10.1002/0471266965.com068.

LITERATURE CITED

Ahmed, N., Agool, I. R., Wright, M. G., Mitchell, K., Koohian, A., Adams, S. J. A., Pidgeon, C. R., Cavenett, B. C., Stanley, C. R., and Kean, A. H. 1992. Far-infrared optically detected cyclotron resonance in GaAs layers and low-dimensional structures. *Semicond. Sci. Technol.* 7:357–363.

Aschcroft, N. W. and Mermin, N. D. 1976. Solid State Physics. Holt, Rinehart and Winston, Philadelphia.

Azbel, M. Ya. and Kaner, E. A. 1958. Cyclotron resonance in metals. *J. Phys. Chem. Solids* 6:113–135.

Born, M. and Wolf, E. 1999. Principles of Optics. Cambridge University Press, Cambridge.

Bowers, R. and Yafet, Y. 1959. Magnetic susceptibility of InSb. *Phys. Rev.* 115:1165–1172.

Brau, C. A. 1990. Free-Electron Lasers. Academic Press, San Diego.

Capasso, F., Gmachl, C., Sivco, D. L., and Cho, A. Y. 2002. Quantum cascade lasers. *Phys. Today* 55:34–38.

Cerne, J., Kono, J., Sherwin, M. S., Sundaram, M., Gossard, A. C., and Bauer, G. E. W. 1996. Terahertz dynamics of excitons in GaAs/AlGaAs quantum wells. *Phys. Rev. Lett.* 77:1131–1134.

Chantry, G. W. 1971. Submillimeter Spectroscopy. Academic Press, New York.

Dresselhaus, G., Kip, A. F., and Kittel, C. 1953. Observation of cyclotron resonance in germanium crystals. *Phys. Rev.* 92:827.

Dresselhaus, G., Kip, A. F., and Kittel, C. 1955. Cyclotron resonance of electrons and holes in silicon and germanium crystals. *Phys. Rev.* 98:368–384.

Goodman, J. W. 1996. Introduction to Fourier Optics. McGraw-Hill, New York.

Gornik, E. 1991. Landau emission. In Landau Level Spectroscopy—Vol. 27.2 of Modern Problems in Condensed Matter Sciences (G. Landwehr and E. I. Rashba, eds.), pp. 912–996. Elsevier Science, Amsterdam.

Hebling, J., Hoffmann, M. C., Hwang, H. Y., Yeh, K.-L., and Nelson, K. A. 2010. Observation of non-equilibrium carrier distribution in semiconductors by THz-pump–THz-probe measurements. *Phys. Rev. B* 81:035201.

Hensel, J. C. and Suzuki, K. 1974. Quantum resonances in the valence bands of germanium. II. Cyclotron resonances in uniaxially stressed crystals. *Phys. Rev. B* 9:4219–4257.

Herlach, F. (ed.). 1984. Strong and ultrastrong magnetic fields and their applications. In Topics in Applied Physics, Vol. 57 Springer-Verlag, Berlin.

Ho, I.-C., Guo, X., and Zhang, X.-C. 2010. Design and performance of reflective terahertz air-based-coherent-detection for time-domain spectroscopy. *Opt. Express* 18: 2872–2883.

Huber, R., Schmid, B. A., Kaindl, R. A., and Chemla, D. S. 2008. Femtosecond THz studies of intra-excitonic transitions. *Phys. Stat. Solidi B* 245:1041–1048.

Kawabata, A. 1967. Theory of cyclotron resonance linewidth. *J. Phys. Soc. Jpn.* 23:999–1006.

Kimmitt, M. F. 1970. Far-Infrared Techniques. Pion Limited, London.

Kittel, C. 1987. Quantum Theory of Solids. John Wiley & Sons, New York.

Kono, J., Lee, S. T., Salib, M. S., Herold, G. S., Petrou, A., and McCombe, B. D. 1995. Optically detected far-infrared resonances in doped GaAs quantum wells. *Phys. Rev. B* 52: R8654–R8657.

Kono, J. and Miura, N. 2006. Cyclotron resonance in high magnetic fields. In High Magnetic Fields: Science and Technology, Vol. III (N. Miura and F. Herlach, eds.), pp. 61–90. World Scientific, Singapore.

Kono, J., Miura, N., Takeyama, S., Yokoi, H., Fujimori, N., Nishibayashi, Y., Nakajima, T., Tsuji, K., and Yamanaka, M. 1993. Observation of cyclotron resonance in low-mobility semiconductors using pulsed ultra-high magnetic fields. *Physica B* 184:178–183.

Larrabee, D. C., Khodaparast, G. A., Tittel, F. K., Kono, J., Rochat, M., Ajili, L., Faist, J., Beere, H., Linfield, E., Nakajima, Y., Nakai, M., Sasa, S., Inoue, M., Chung, S. J., and Santos, M. B. 2004. Application of terahertz quantum cascade lasers to semiconductor cyclotron resonance. *Opt. Lett.* 29:122–124.

Lax, B. and Mavroides, J. G. 1960. Cyclotron resonance. In Solid State Physics, Vol. 11 (F. Seitz and D. Turnbull, eds.), pp. 261–400. Academic Press, New York.

Lax, B., Zeiger, H. J., Dexter, R. N., and Rosenblum, E. S. 1953. Directional properties of the cyclotron resonance in germanium. *Phys. Rev.* 93:1418–1420.

Luttinger, J. M. 1951. The effect of a magnetic field on electrons in a periodic potential. *Phys. Rev.* 84:814–817.

Luttinger, J. M. 1956. Quantum theory of cyclotron resonance in semiconductors: General theory. *Phys. Rev.* 102:1030–1041.

Luttinger, J. M. and Kohn, W. 1955. Motion of electrons and holes in perturbed periodic fields. *Phys. Rev.* 97: 869–883.

Mavroides, J. G. 1972. Magneto-optical properties. In Optical Properties of Solids (F. Abeles, ed.), pp. 351–528. North-Holland, Amsterdam.

McCombe, B. D. and Wagner, R. J. 1975. Intraband magneto-optical studies of semiconductors in the far-infrared. In Advances in Electronics and Electron Physics (L. Marton, ed.), Vol. 37, pp. 1–78, and Vol. 38, pp. 1–53. Academic Press, New York.

Michels, J. G., Warburton, R. J., Nicholas, R. J., and Stanley, C. R. 1994. An optically detected cyclotron resonance study of bulk GaAs. *Semicond. Sci. Technol.* 9:198–206.

Mittleman, D. (ed.). 2002. Sensing with Terahertz Radiation. Springer-Verlag, Berlin.

Miura, N. 1984. Infrared magnetooptical spectroscopy in semiconductors and magnetic materials in high pulsed magnetic fields. In Infrared and Millimeter Waves, Vol. 12 (K. J. Button, ed.), pp. 73–143. Academic Press, New York.

Nicholas, R. J. 1994. Intraband optical properties of low-dimensional semiconductor systems. In Handbook on Semiconductors, Vol. 2 "Optical Properties" (M. Balkanski, ed.), pp. 385–461. Elsevier, Amsterdam.

Nuss, M. C. and Orenstein, J. 1998. Terahertz time-domain spectroscopy. In Millimeter and Submillimeter Wave Spectroscopy of Solids (G. Grüner, ed.), pp. 7–44. Springer-Verlag, Berlin.

Otsuka, E. 1991. Cyclotron resonance. In Landau Level Spectroscopy—Vol. 27.1 of Modern Problems in Condensed Matter Sciences (G. Landwehr and E. I. Rashba, eds.), pp. 1–78. Elsevier Science, Amsterdam.

Palik, E. D. and Furdyna, J. K. 1970. Infrared and microwave magnetoplasma effects in semiconductors. Rep. Prog. Phys. 33:1193–1322.

Petrou, A. and McCombe, B. D. 1991. Magnetospectroscopy of confined semiconductor systems. In Landau Level Spectroscopy—Vol. 27.2 of Modern Problems in Condensed Matter Sciences (G. Landwehr and E. I. Rashba, eds.), pp. 679–775. Elsevier Science, Amsterdam.

Pidgeon, C. R. 1994. Free carrier Landau level absorption and emission in semiconductors. In Handbook on Semiconductors, Vol. 2 "Optical Properties" (M. Balkanski, ed.), pp. 637–678. Elsevier, Amsterdam.

Pidgeon, C. R. and Brown, R. N. 1966. Interband magnetoabsorption and Faraday rotation in InSb. Phys. Rev. 146:575–583.

Rubens, H. and von Baeyer, O. 1911. On extremely long waves, emitted by the quartz mercury lamp. Philos. Mag. 21:689–695.

Sakai, K. (ed.). 2005. Terahertz Optoelectronics. Springer, Berlin.

Sakurai, J. J. 1985. Modern Quantum Mechanics. Addison-Wesley Publishing Co., Redwood City, CA.

Salib, M. S., Nickel, H. A., Herold, G. S., Petrou, A., McCombe, B. D., Chen, R., Bajaj, K. K., and Schaff, W. 1996. Observation of internal transitions of confined excitons in GaAs/AlGaAs quantum wells. Phys. Rev. Lett. 77:1135–1138.

Slater, J. C. 1949. Electrons in perturbed periodic lattices. Phys. Rev. 76:1592–1601.

Stewart, J. E. 1970. Infrared Spectroscopy. Marcel Dekker, New York.

Suzuki, K. and Hensel, J. C. 1974. Quantum resonances in the valence bands of germanium. I. Theoretical considerations. Phys. Rev. B 9:4184–4218.

Wang, X., Hilton, D. J., Ren, L., Mittleman, D. M., Kono, J., and Reno, J. L. 2007. Terahertz time-domain magnetospectroscopy of a high-mobility two-dimensional electron gas. Opt. Lett. 32:1845–1847.

Wang, X., Hilton, D. J., Reno, J. L., Mittleman, D. M., and Kono, J. 2010. Direct measurement of cyclotron coherence times of high-mobility two-dimensional electron gases. Opt. Express 18:12354–12361.

Wannier, G. H. 1937. The structure of electronic excitation levels in insulating crystals. Phys. Rev. 52:191–197.

Williams, B. S. 2007. Terahertz quantum-cascade lasers. Nat. Photonics 1:517–525.

Wright, M. G., Ahmed, N., Koohian, A., Mitchell, K., Johnson, G. R., Cavenett, B. C., Pidgeon, C. R., Stanley, C. R., and Kean,

A. H. 1990. Far-infrared optically detected cyclotron resonance observation of quantum effects in GaAs. Semicond. Sci. Technol. 5:438–441.

Zeiger, H. J., Rauch, C. J., and Behrndt, M. E. 1959. Cross modulation of D. C. resistance by microwave cyclotron resonance. Phys. Chem. Solids 8:496–498.

KEY REFERENCES

Dresselhaus et al., 1955. See above.

This seminal article is still a useful reference not only for CR spectroscopists but also for students beginning to study semiconductor physics. Both experimental and theoretical aspects of CR in solids as well as the band structure of these two fundamental semiconductors (Si and Ge) are described in great detail.

Landwehr, G. and Rashba, E. I. (eds.). 1991. Landau Level Spectroscopy—Vol. 27.1 and 27.2 of Modern Problems in Condensed Matter Sciences. Elsevier Science, Amsterdam.

These two volumes contain a number of excellent review articles on magneto-optical and magnetotransport phenomena in bulk semiconductors and low-dimensional semiconductor quantum structures.

Lax and Mavroides, 1960. See above.

This review article provides a thorough overview on early, primarily microwave, CR studies in the 1950s. A historical discussion is given also of CR of electrons and ions in ionized gases, which had been extensively investigated before CR in solids was first observed.

McCombe and Wagner, 1975. See above.

Describes a wide variety of far infrared magneto-optical phenomena observed in bulk semiconductors in the 1960s and 1970s. Detailed descriptions are given to basic theoretical formulations and experimental techniques as well as extensive coverage of experimental results.

✛

MÖSSBAUER SPECTROMETRY

Brent Fultz

Department of Applied Physics and Materials Science, California Institute of Technology, Pasadena, CA, USA

INTRODUCTION

Mössbauer spectrometry is based on the quantum mechanical "Mössbauer effect," which provides a non-intuitive link between nuclear and solid-state physics. Mössbauer spectrometery measures the spectrum of energies at which specific nuclei absorb γ rays. Curiously, for one nucleus to emit a γ ray and a second nucleus to absorb it with efficiency, the atoms containing the two nuclei must be bonded chemically in solids. A young Rudolf Mössbauer observed this efficient γ-ray emission and absorption process in ^{191}Ir, and explained why the nuclei must be embedded in solids. Mössbauer spectrometry is now performed primarily with the nuclei